Monthly Notices of the ROYAL ASTRONOMICAL SOCIETY

MNRAS **495,** 1724–1736 (2020)
Advance Access publication 2020 April 2

doi:10.1093/mnras/staa657

SuperCLASS – II. Photometric redshifts and characteristics of spatially resolved μJy radio sources

Sinclaire M. Manning,[1★] Caitlin M. Casey,[1] Chao-Ling Hung,[2] Richard Battye,[3] Michael L. Brown,[3] Neal Jackson,[3] Filipe Abdalla,[4] Scott Chapman,[5] Constantinos Demetroullas,[3,6] Patrick Drew,[1] Christopher A. Hales,[7,8] Ian Harrison,[3,9] Christopher J. Riseley,[10,11,12] David B. Sanders[13] and Robert A. Watson[3]

[1] *Department of Astronomy, The University of Texas at Austin, 2515 Speedway Boulevard Stop C1400, Austin, TX 78712, USA*
[2] *Physics Department, Manhattan College, 4513 Manhattan College Pkwy, Bronx, NY 10471, USA*
[3] *Jodrell Bank Centre for Astrophysics, Department of Physics and Astronomy, The University of Manchester, Manchester M13 9PL, UK*
[4] *Department of Physics and Astronomy, University College London, Gower Place, London WC1E 6BT, UK*
[5] *Department of Physics and Atmospheric Science, Dalhousie University, Halifax, NS B3H 4R2, Canada*
[6] *Cyprus University of Technology, Archiepiskopou Kyprianou 30, Limassol 3036, Cyprus*
[7] *National, Radio Astronomy Observatory, P.O. Box 0, Socorro, NM 87801, USA*
[8] *School of Mathematics, Statistics and Physics, Newcastle University, Newcastle upon Tyne NE1 7RU, UK*
[9] *Department of Physics, University of Oxford, Denys Wilkinson Building, Keble Road, Oxford OX1 3RH, UK*
[10] *Dipartimento di Fisica e Astronomia, Università degli Studi di Bologna, via P. Gobetti 93/2, I-40129 Bologna, Italy*
[11] *INAF – Istituto di Radioastronomia, via P. Gobetti 101, I-40129 Bologna, Italy*
[12] *CSIRO Astronomy and Space Science, P.O. Box 1130, Bentley, WA 6102, Australia*
[13] *Institute for Astronomy, University of Hawaii, 2680 Woodlawn Drive, Honolulu, HI 96822, USA*

Accepted 2020 March 1. Received 2020 February 26; in original form 2019 November 21

ABSTRACT

We present optical and near-infrared imaging covering a $\sim$1.53 deg^2 region in the Super-Cluster Assisted Shear Survey (SuperCLASS) field, which aims to make the first robust weak lensing measurement at radio wavelengths. We derive photometric redshifts for $\approx$176 000 sources down to $i'_{\rm AB} \sim 24$ and present photometric redshifts for 1.4 GHz expanded Multi-Element Radio Linked Interferometer Network (*e*-MERLIN) and Karl G. Jansky Very Large Array (VLA) detected radio sources found in the central 0.26 deg^2. We compile an initial catalogue of 149 radio sources brighter than $S_{1.4} > 75$ μJy and find their photometric redshifts span $0 < z_{\rm phot} < 4$ with radio luminosities between 10^{21} and 10^{25} W Hz^{-1}, with medians of $\langle z \rangle = 0.55$ and $\langle L_{1.4} \rangle = 1.9 \times 10^{23}$ W Hz^{-1}, respectively. We find 95 per cent of the μJy radio source sample (141/149) have spectral energy distributions (SEDs) best fit by star-forming templates while 5 per cent (8/149) are better fit by active galactic nuclei (AGN). Spectral indices are calculated for sources with radio observations from the VLA and Giant Metrewave Radio Telescope (GMRT) at 325 MHz, with an average spectral slope of $\alpha = 0.59 \pm 0.04$. Using the full photometric redshift catalogue, we construct a density map at the redshift of the known galaxy clusters, $z = 0.20 \pm 0.08$. Four of the five clusters are prominently detected at $> 7\,\sigma$ in the density map and we confirm the photometric redshifts are consistent with previously measured spectra from a few galaxies at the cluster centres.

Key words: galaxies: distances and redshifts – galaxies: photometry – cosmology: observations.

1 INTRODUCTION

As direct probes of obscured star formation, infrared (IR) through radio wavelength observations provide crucial insight into the formation and evolution of galaxies across cosmic time. Galaxies with IR luminosities around $10^{12} \sim 10^{13}$ L$_\odot$ from 8 to 1000 μm have estimated star formation rates (SFRs) of hundreds to thousands of solar masses per year and represent the most intense starbursts in the Universe (e.g. Smail, Ivison & Blain 1997; Chapman et al. 2005). Surveys from the *Herschel Space Observatory* tell us that these

★ E-mail: smanning@astro.as.utexas.edu

galaxies contribute significantly to the total cosmic star formation history, providing at least half of the Universe's star formation at its peak at $z \sim 2$ (Casey et al. 2012; Gruppioni et al. 2013; Madau & Dickinson 2014).

The population of dusty star-forming galaxies (DSFGs; Casey, Narayanan & Cooray 2014) relates closely to the μJy radio source population (e.g. Chapman et al. 2003; Barger, Cowie & Wang 2007). For the purposes of this work μJy radio sources are galaxies with 1.4 GHz flux densities between 10–1000 μJy whose radio emission is most likely dominated by synchrotron emission from supernova remnants, which closely tracks their SFRs (Helou, Soifer & Rowan-Robinson 1985). However, placing meaningful constraints on the physical origins and drivers of the intense star formation in these systems has been difficult. This is due to the significant obscuration at optical/near-infrared (OIR) wavelengths caused by dust formed in these galaxies' star-forming regions (Magnelli et al. 2009; Whitaker et al. 2017). For example, it is still unclear from both observations (Tacconi et al. 2008; Engel et al. 2010; Ivison et al. 2012; Hodge et al. 2012) and theory (Dekel, Sari & Ceverino 2009; Davé et al. 2010; Narayanan et al. 2010, 2015) whether this enhanced star formation in DSFGs/μJy radio sources is triggered by a steady build up of material via cold gas accretion or short bursts via mergers.

The expanded Multi-Element Radio Linked Interferometer Network (*e*-MERLIN) is a network of seven UK-based radio telescopes designed for high spatial resolution ∼GHz observations. With a maximum baseline of 217 km, corresponding to a resolution of ≈200 mas at 1.4 GHz, the facility's unique combination of sensitivity and spatial resolution makes it an ideal tool to trace spatially resolved star formation in heavily obscured galaxies like the μJy radio source population. *e*-MERLIN is the only radio telescope capable of resolving the internal, unobscured star formation within a statistically significant population of high-redshift galaxies as it is a dedicated long-baseline facility. *e*-MERLIN has embarked on an ambitious ∼1 deg^2, high-resolution (0.3 arcsec), 1.4 GHz (L-band) radio continuum survey of a new extragalactic deep field, called the Super-Cluster Assisted Shear Survey (SuperCLASS) using 832 h of observations.

SuperCLASS (Paper I in this series) is a deep, wide-area survey using the *e*-MERLIN interferometric array designed to detect the effects of weak lensing in radio continuum in a supercluster region where there are five $z \sim 0.2$ Abell galaxy clusters already identified (Abell, Corwin & Olowin 1989; Struble & Rood 1999). The SuperCLASS survey's primary science goals are to: (1) provide a test-bed for weak lensing studies at radio wavelengths for the future Square Kilometer Array (SKA) and other SKA progenitors and (2) obtain internal ∼kpc maps of μJy radio sources for statistically large samples, determining their evolutionary origins through morphological analysis. High-resolution *e*-MERLIN imaging combined with observations from the Karl G. Jansky Very Large Array (VLA) provides results similar to that expected of the SKA, allowing for the development of the tools required for shape measurement and a quantitative assessment of the physical properties of radio sources that can be used for cosmic shear measurements (Brown & Battye 2011; Harrison et al. 2016; Bonaldi et al. 2016; Camera et al. 2017).

This paper presents the initial catalogue of photometric redshifts as measured via new optical and near-IR imaging data for SuperCLASS obtained from Subaru and *Spitzer*. With these data, we present an initial analysis of radio-detected galaxies in the field and the distribution of galaxies in and around the five $z \sim 0.2$ Abell galaxy clusters. We outline the individual data sets compiled for the survey in Section 2 and we describe the methods used

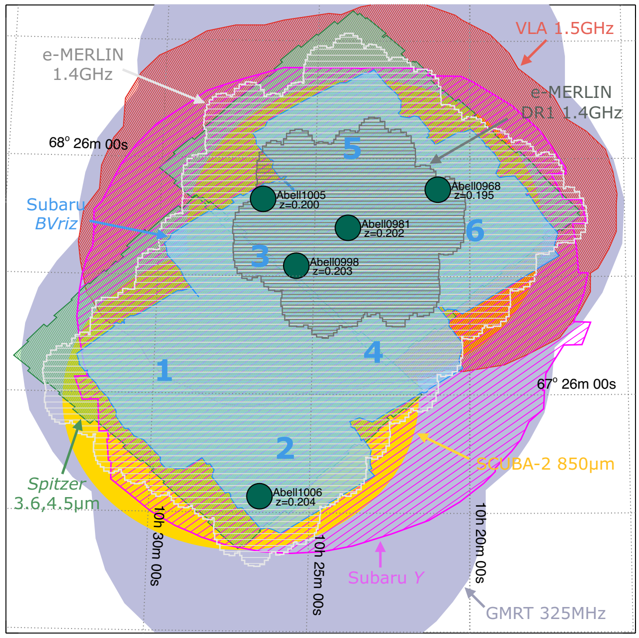

Figure 1. SuperCLASS coverage map showing all collected observations, plus the full proposed *e*-MERLIN field (white). The six footprints covered by Subaru SC *BVriz* are shown in blue, Subaru HSC *Y*-band in magenta, *Spitzer* 3.6 and 4.5 μm data in green, SCUBA-2 850 μm in yellow, GMRT 325 MHz data in lavender, the *e*-MERLIN 1.4 GHz DR1 in dark grey, and VLA 1.5 GHz in red.

to measure photometric redshifts in Section 3. We discuss the redshift distribution of radio sources and distribution of sources surrounding the field's galaxy clusters are presented in Section 5. Section 6 summarizes our results. We assume a *Planck* Λ-cold dark matter cosmology with $\Omega_m = 0.307$ and $H_0 = 67.7\,\mathrm{km\,s^{-1}\,Mpc^{-1}}$ (Collaboration et al. 2016).

2 DATA AND OBSERVATIONS

What follows is a description of the core data products of the SuperCLASS survey, from the optical through near-IR, to radio observations. The optical and near-IR data are used to estimate photometric redshifts, while the *e*-MERLIN/VLA data are used for a discussion of physical characteristics of the radio luminous sample. For a more thorough overview of the radio survey data sets in SuperCLASS, we refer the reader to Paper I (*e*-MERLIN and VLA) and Riseley et al. (2016) for the GMRT data. Paper III provides an initial analysis of the weak lensing signal in the field. Fig. 1 provides a visual summary of the SuperCLASS survey as it currently stands as well as the positions of the five Abell clusters, which together constitute a supercluster at $z \sim 0.2$.

2.1 Subaru optical imaging

Deep photometric data in the optical bands *BVriz* were obtained using Suprime-Cam (SC) on the Subaru 8.4 m telescope on Maunakea on 2013 February 5 and 6 (PI: Casey). Most of the second night (February 6) was lost due to poor weather and cloud cover. Seeing ranged from 1.0 to 1.4 arcsec. The SC data are comprised of six observed subfields, each with a field of view (FOV) of 34 arcmin × 27 arcmin, covering 1.53 deg^2 total. Individual and total exposure times in these bands were: 200 s, totaling 1000 s for all six footprints

Table 1. SC footprint info.

Footprint	RA	Dec.	PA
1	10:30:38.8	+67:30:18.2	33.5°
2	10:27:07.1	+67:16:00.2	33.8°
3	10:27:23.5	+67:56:35.9	33.3°
4	10:23:50.9	+67:42:14.4	33.3°
5	10:24:04.7	+68:22:46.6	33.9°
6	10:20:31.2	+68:08:21.5	33.7°

Note: Position centroids and position angles of the six Subaru SC footprints.

(*B* and *V*); 150 s, totaling 750 s for all six footprints (r'); 200 s, totaling 2000 s for all six footprints (i'); 240 s, totaling 1200 s for footprints 1–3 and 361.5 s for footprint 4 (z'). Table 1 gives the position centroids for the six footprints and their position angles east of north about the centroid.

Y-band imaging was obtained using Hyper Suprime-Cam (HSC) on 2015 March 27 (PI: Hung). HSC has a 90 arcmin diameter FOV. Total integration time for the northeast image was 106 and 96 min for the southwest. Seeing varied between 0.61 and 1.25 arcsec for the individual HSC exposures. There are ∼195 000 sources with $Y < 24.3$ which we deem as a reliable counterpart match to our catalogue generated from SC data, to be discussed later in this section. The inclusion of this filter proves useful as it probes key colors of both the $z = 0.2$ population as well as the high-z tail in which we are interested.

Due to the differences in seeing, conditions, and exposure times between the *BVrizY* optical images, we convolve all images with a matched point spread function (PSF) to perform multiband photometry and eliminate all resolution discrepancies. PSF matching is crucial for accurate estimations of colours (Capak et al. 2007) as otherwise aperture differences can significantly impact photometric redshift estimation. To do this, we use the SC image with the worst seeing (1.38 arcsec, full-width half maximum, FWHM) as our reference PSF and create a PSF kernel. The kernel is then convolved with the remaining SC and HSC images to match the PSF of the reference image following standard procedure.

We use Source Extractor (SExtractor; Bertin & Arnouts 1996) to build a catalogue of objects from the PSF matched Subaru images and extract positions, magnitudes, and associated errors of the sources in the field. SExtractor subtracts the estimated background from the photometry and uses the root mean square (rms) to estimate errors. We find the uncertainties to be underestimated by a factor of 10 based on the noise in the images and thus add a floor of 0.01 to the errors to account for this. We apply an aperture size with a 15 pixel diameter (3 arcsec), a minimum detection area of 3 pixels, and 3 σ detection threshold in the SExtractor parameters to detect sources. We run SExtractor in dual-image mode in which a deep, co-added image from all optical filters is used for object detection (Capak et al. 2007; Laigle et al. 2016). Forced photometry is then measured from each individual filter image. This procedure allows for the same aperture to be applied across all filters and objects are automatically matched, providing straightforward comparisons and cross-matching between different bands. A background rms map with a mesh size of 12.8 arcsec is created and applied allowing for SExtractor to reduce the number of spurious detections.

The northernmost 1/3 of the field lacks z'-band data due to on the fly decisions made while observing; at the time, the *e*-MERLIN coverage area was planned to extend across the full 1.53 deg^2. Unfortunately, this 1/3 of the field encompasses where the deepest *e*-MERLIN map sits. The impact of lack of z'-band coverage on the reliability of the photometric redshifts is discussed further in Section 3.

The Subaru images are then flux calibrated using known stars in the large FOV. The FOV of both SC and HSC data sets is sufficiently large to have standard stars within our science frames. We make use of the Data Release 1 (DR1) Pan-STARRS (Panoramic Survey Telescope And Rapid Response System) 3π survey (Chambers et al. 2016) as our astrometry and photometry reference down to AB < 22. Non-linear astrometric warps are corrected with astrometry.net (Lang 2009). To flux calibrate, we take a sample of 1192 unsaturated stars across all six footprints in both SC/HSC and PS1 3π with magnitudes between 15 and 19. We colour correct from PS1 *grizy* to our *BVrizY* bands using stellar templates from the Stellar Spectral Flux Library (Pickles 1998), convolving them with the spectral response functions (including atmosphere, detector throughput, and quantum efficiency) of the Subaru filters, and compare their magnitudes across filter sets. We then identify the best-fitting stellar models for each observed star using a χ^2 minimization technique and determine a global offset to be applied to flux calibrate. This is folded into our catalogur generation via the `MAG_ZEROPOINT` parameter in the SExtractor configuration file.

Some sources may be detected in more than one Subaru image due to spatial overlap between the six footprints. We identify duplicate detections and calculate the inverse-variance weighted average of the magnitudes so as to make use of all available data. This results in a master catalogue of 376 380 objects, but after downselecting based on the i'-band 90 per cent completeness limit ($i' < 24.5$), we end up with 176 447 sources. This work broadly agrees with expected optical number counts (Nagashima et al. 2002). Fig. 2 shows the 90 per cent completeness limits and 5 σ detection thresholds for these optical and near-IR observations. We calculate our completeness limits using a linear approximation of log(*N*) extrapolating down to 90 per cent. The use of a co-added detection image during source extraction results in an increased number of faint object detections and therefore we do not see the steep drop off in the number counts that is expected. The thick grey line shows the i'-band number count without using a detection image and here we recover the typical profile. We note that the single-filter i'-band images are noisier compared to the smooth, psf-matched co-added image. As such, we boost the detection threshold and minimum detections area to 5 σ and 10 pixels respectively to decrease the number of contaminants. There still exists an excess in the single filter number counts between 25 and 26 i'-band magnitude, but this can be attributed to spurious detections around image edges, stellar diffraction, and noise spikes. Table 2 breaks down this information by the Subaru footprint for the optical and near-IR data.

2.2 Near-infrared observations

The SuperCLASS field was observed for 12.7 h with the *Spitzer* Infrared Array Camera (IRAC) at 3.6 μm (*M* band) and 4.5 μm (*N* band) during Cycle 12 in program number 12074 (PI: Casey). Flux calibration was completed using astronomical standard stars in *Spitzer*'s continuous viewing zone and that were monitored throughout observations. Data were reduced and processed with the basic calibrated data (BCD) pipeline and post-BCD software. Sources were extracted using SExtractor accounting for the large point response function (PRF), 1.78 arcsec for the 3.6 μm channel and 1.80 arcsec for the 4.5 μm channel. No prior positions were used for *Spitzer* source extraction and detections were treated as independent from sources identified in the optical bands. Imaging reached a 5 σ point source sensitivity limit of 21.1 mag at both 3.6

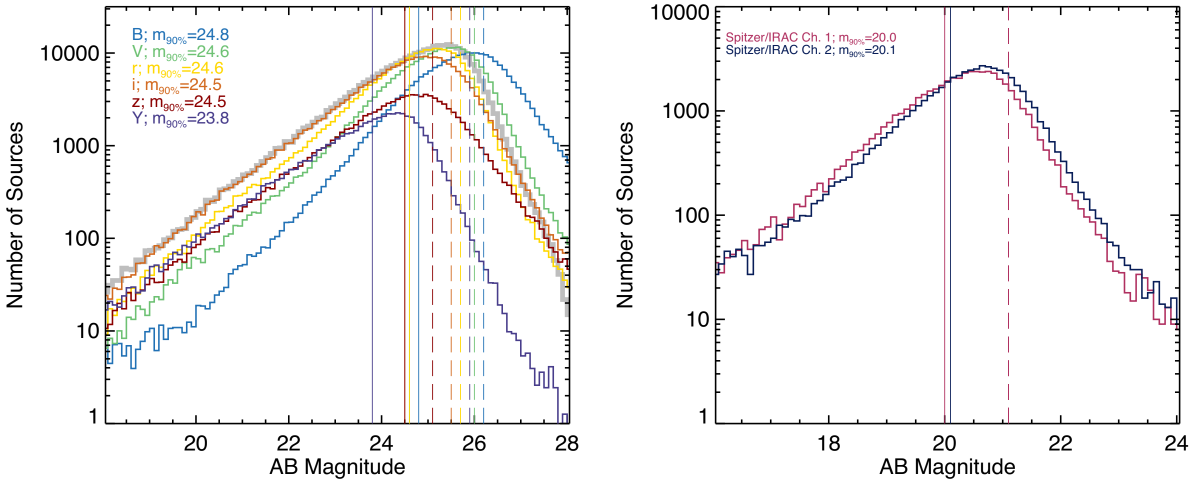

Figure 2. Aggregate differential number counts showing image depth and completeness for the optical Subaru *BVrizY* (left) and *Spitzer* 3.6 and 4.5 µm observations (right). Vertical solid lines show at what depth we are 90 per cent complete in our sample in each photometric filter and dashed lines show the 5 σ detection thresholds. The thick grey line shows the i'-band number count using the single filter image rather than the co-added detection image. The *Spitzer* 3.6 and 4.5 µm 5 σ detection limits are both 21.1 mag.

Table 2. OIR completeness.

Footprint	Filter	5σ detection threshold	90 per cent completeness
1	*B*	26.1	24.9
1	*V*	26.1	24.9
1	r'	26.0	24.8
1	i'	25.7	24.6
1	z'	24.9	24.6
2	*B*	26.1	24.8
2	*V*	25.5	24.7
2	r'	25.6	24.6
2	i'	25.2	24.7
2	z'	25.0	24.5
3	*B*	26.1	24.8
3	*V*	26.0	24.7
3	r'	26.2	24.5
3	i'	25.9	24.5
3	z'	25.4	24.4
4	*B*	26.3	24.9
4	*V*	26.1	24.6
4	r'	25.9	24.5
4	i'	25.8	24.5
5	*B*	26.3	24.8
5	*V*	26.3	24.3
5	r'	25.2	24.6
5	i'	25.2	24.6
6	*B*	26.3	24.8
6	*V*	26.1	24.6
6	r'	25.2	24.6
6	i'	25.2	24.6
Full field	*Y*	25.9	23.8
Full field	[3.6]	21.1	20.0
Full field	[4.5]	21.1	20.1

Notes: List of 5σ detection thresholds and 90 per cent completeness limits for each photometric band, sorted by footprint. z'-band data are currently only available for footprints 1–3.

and 4.5 µm. Catalogues are approximated to be 90 per cent complete down to 20.0 and 20.1, respectively, finding ≈82 000 and ≈83 000 sources in the two filters across the survey. Source positions are matched to the optical catalogue with a nearest neighbour radius of 1 arcsec. The spherical distance to the nearest optical sources is 0.3 arcsec and after injecting 80 000 fake sources into the *Spitzer* field we find a false match contamination rate of 1.25 per cent.

Near-IR *K*-band observations of the SuperCLASS field were obtained with the Wide-field InfraRed Camera (WIRCAM) on the Canada–France–Hawaii Telescope (PI: Chapman). Images reached moderate depth (AB < 19), but unfortunately a key section of the field (encompassing the DR1 *e*-MERLIN field) lacks coverage. Because of this gap in observations and relatively shallow and non-uniform depth, *K*-band photometry is not included in the photometric redshift analysis outlined in Section 3.

2.3 *L*-band and other radio observations

The *e*-MERLIN observations consist of 112 pointings, of which 49 have been observed, making up the the current 0.26 deg^2 DR1 area. Each pointing was observed for 400 mi in total with an rms sensitivity of 15 µJy at 1.4 GHz. This region includes four of the five Abell clusters (A968, A981, A998, and A1005). Observations were performed in units of 15 h over the frequency range 1.204–1.717 GHz. The bandwidth was divided into 8 Intermediate Frequencies (IFs), each of 512 channels of 125 kHz width to give an unsmeared FOV of 30 arcmin, sufficient to map the whole primary beam of the smallest (25 m diameter) telescopes in the *e*-MERLIN array. Observations began 2014 December 29, continuing into 2015 and 2016. Data were reduced with a modified version of the National Radio Astronomy Observatory (NRAO) AIPS package and cleaned of radio frequency interference (RFI) using a similar algorithm to the AOFlagger program (Offringa 2010; Offringa et al. 2010). In Fig. 1, the dark grey area shows the completed observations of the DR1 region and white encompasses the full field as well as the proposed extension to the south which would increase the survey area to ∼ 2 deg^2 and include the fifth cluster. Please refer to Paper I in this series for more detailed discussion of the first radio DR.

In addition, 24 h of *L*-band (1.5 GHz) observations (112 pointings) were taken using the VLA in A configuration in 2015 August under project code 15A-053 (PI: Battye) to complement the *e*-MERLIN observations. The total observing time was divided into 6 × 4 h sessions and were assigned staggered local sidereal time (LST) start times to maximize coverage in the *u*–*v* plane. These observations yielded an rms noise typically less than 7 μJy beam^{-1} across the mosaic.

Low-frequency 325 MHz observations were carried out using the Giant Metrewave Radio Telescope (GMRT, PI: Scaife) covering a ∼ 6.5 deg^2 FOV, achieving a nominal sensitivity of 34 μJy beam^{-1}. From these data, a catalogue of 3257 sources with flux densities in the range of 183 μJy–1.5 Jy was compiled (Riseley et al. 2016); 454 of these sources lie in the DR1 field.

3 PHOTOMETRIC REDSHIFTS

3.1 Photometric redshift fitting

We use the Easy and Accurate Z-phot from Yale (EAZY; Brammer, van Dokkum & Coppi 2008) to calculate photometric redshifts across the SuperCLASS field. EAZY is optimized for galaxy samples lacking spectroscopic information with the default settings optimized to work with multiwavelength photometric data alone, though spectroscopic redshifts can be included for photometric redshift calibration if available. EAZY also includes dusty starburst models as part of its template set, an important addition considering our interest in DSFGs.

The template set provided by EAZY (v1.3 which includes a dusty starburst model) is a linear combination of ∼ 500 (Bruzual & Charlot 2003, BC03) synthetic galaxy photometry models which are then used to create eight ‘basis’ templates. These eight templates are then combined using weighting coefficients to create a representative sample of galaxy spectral energy distributions (SEDs) over a broad redshift range. The algorithm steps through a grid of redshifts ($0 < z < 6$) and at each redshift finds the best-fitting synthetic template spectrum. Using EAZY, we obtain the best-fitting SED generated from the template set, the photometric redshift probability distribution, and the minimum χ^2 distribution as a function of redshift for the best-fitting template for each source. We show five example galaxies with good photometric redshift fits ranging from $0.2 < z < 3.1$ in Fig. 3.

Duncan et al. (2018) showed that some improvement in the photometric redshift estimation for radio sources is possible using alternative template sets within EAZY, particularly the ATLAS (Brown et al. 2014) and XMM-COSMOS (Salvato et al. 2009, 2011) templates. The current EAZY template set only models stellar emission and does not include any contribution from active galactic nucleus (AGN, e.g. contribution from AGN continuum emission or broad emission lines), which could result in inaccurate redshift fits for our radio source population. Both the radio source population and the potential AGNs are of interest to us for both accurate redshifts for weak lensing and galaxy evolution analysis. Thus, we also use the XMM-COSMOS template set to run an independent test of photometric redshifts for all sources for comparison.

In the central DR1 SuperCLASS map 154 *e*-MERLIN/VLA μJy radio sources are identified. Of these sources, 149 (∼ 97 per cent) have good or moderate quality photometric redshift solutions with $\Delta z_{\rm phot}/(1 + z_{\rm phot}) < 1$, where $\Delta z_{\rm phot} = z_{\rm u68} - z_{\rm l68}$. We opt against using a stronger cut because of the limited number of filters. The five remaining radio sources have highly degenerate photometric redshift solutions spanning a wide redshift range. For the 149 sources with converged photometric redshift fits, we visually inspect the SEDs produced from the star-forming templates (BC03) and AGN templates (*XMM*) to determine the best-fitting solution. We refrain from using minimum χ^2 values to compare the fits using BC03 or *XMM* due to the different number of free parameters in their respective photometric redshift determinations. A few cases do not have substantially better fits in either the BC03 or *XMM* template set. While the majority of these exhibit similar redshift solutions, a few do not. An example of one such source is illustrated in Fig. 4. In cases such as this, we defer to the BC03 fit given the range of radio flux densities in our sample and the lower anticipated source density of AGN, but keep track of these cases and a future paper will further explore their photometry and morphologies to infer a more accurate constraint.

The redshift distribution for all 176 000+ OIR sources in the ∼ 1.53 deg^2 field appears to show a deficit of sources between $1 < z_{\rm phot} < 2$ and an excess at $z_{\rm phot} < 1$ relative to fields with well-characterized photometric redshifts (e.g. COSMOS; Laigle et al. 2016). To determine the origin of these discrepancies, we employ a mock catalogue of galaxies from cosmological simulations to examine the effectiveness of our filter set in recovering photometric redshifts (Section 4).

3.2 Assessing photometric redshift errors via close pairs

Following the work of Quadri & Williams (2010) and Bezanson et al. (2016), we determine the scatter in our photometric redshifts from an analysis of close pairs to provide confidence in the precision of the estimates presented in this paper. As stated in these works, galaxies which appear near to each other (2.5–15 arcsec separation) are likely to be physically associated thanks to the clustered nature of galaxies. If we assume both galaxies in a projected pair are at the same redshift, then any discrepancy between the two measured redshifts will be due to an error in the measurements and fitting procedure. This close pairs analysis allows for an independent test of the photometric redshift accuracy which is necessary considering the lack of spectroscopic redshifts available for comparison in our sample.

Errors on the photometric redshifts of the close pairs are related to the Gaussian distribution of their redshift deviations (equation 2 of Bezanson et al. 2016) and we adopt a separation range of 2.5–15 arcsec to determine pairs. From the distribution of redshift separations for galaxy pairs, we then subtract the distribution created using a catalogue in which the galaxy positions have been randomized in order to estimate the contribution from chance projections. After fitting a Gaussian to the new distribution accounting for uncorrelated pairs, we determine the representative photometric redshift scatter, $\sigma_{\rm pairs}/\sqrt{2} = 0.11$, to be in line with our measured uncertainties which are 0.08 on average.

3.3 Photometric redshift priors with COSMOS

Based on the assumption that the μJy radio source redshift distribution is similar across all areas of the sky, we use the well-constrained photometric redshifts for 1.4 GHz radio galaxies from the COSMOS field (Laigle et al. 2016) as priors to weight the probability distribution functions (PDFs) generated for the 154 *e*-MERLIN detected radio sources by EAZY. For each source, we find all sources in the COSMOS catalogue that have similar VLA 1.4 GHz flux densities and 3.6 μm magnitudes (within 5 per cent). We then construct a redshift distribution, taking the individual PDFs from COSMOS photometry into account, and multiply it by the EAZY PDF to obtain a redshift distribution based on the prior as matched to the COSMOS sample. Six out of 149 radio sources do

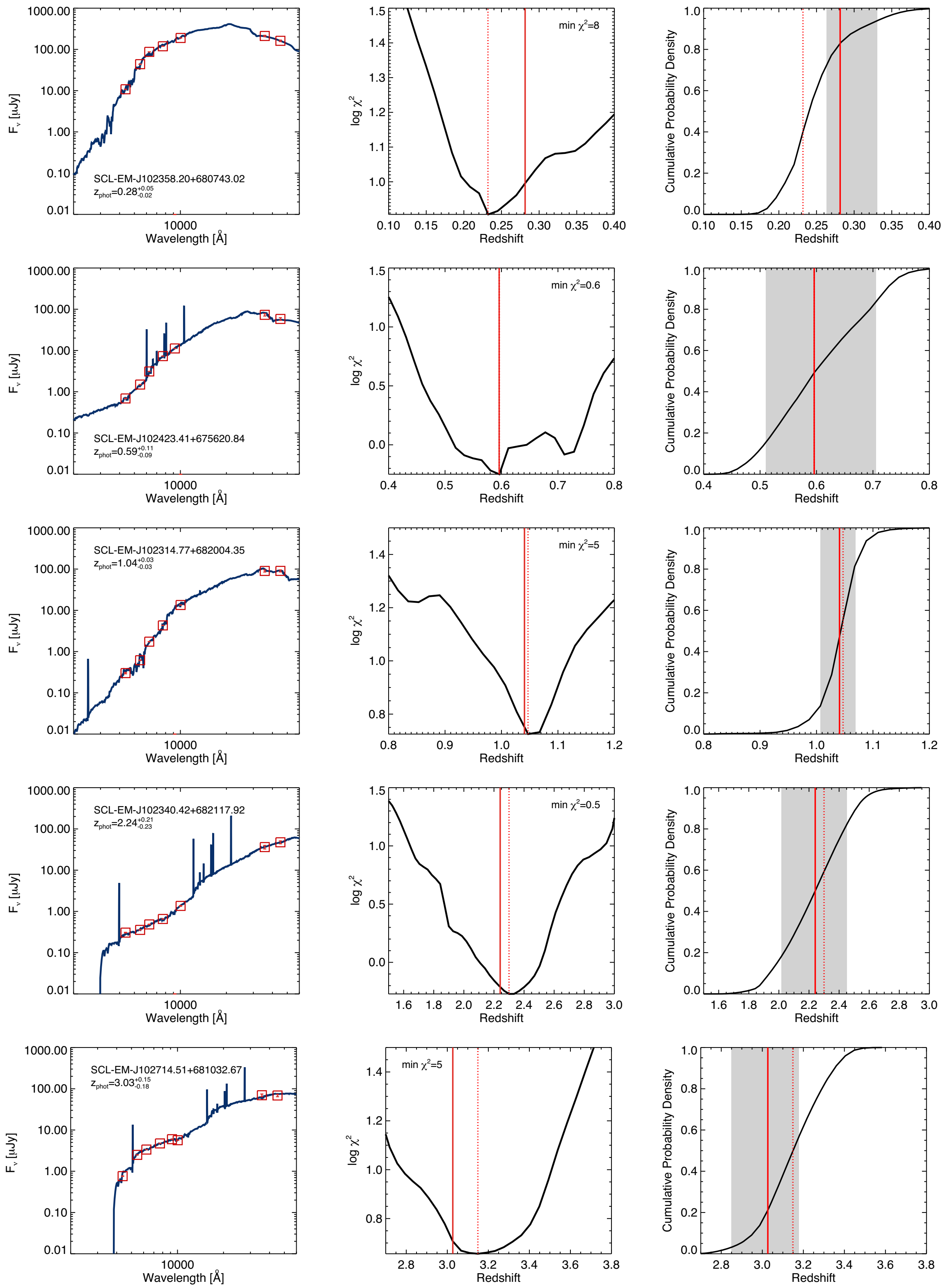

Figure 3. Example SED fit to SuperCLASS galaxy photometry (left), χ^2 distribution of the best-fitting star-forming template sets (centre), and cumulative probability density function (right), for five sources with $0 < z_{\rm phot} < 4$. Dotted red lines show the photometric redshift solution corresponding to the minimum χ^2. Solid red lines mark photometric redshifts after the COSMOS priors are applied and their corresponding 1 σ confidence intervals in grey.

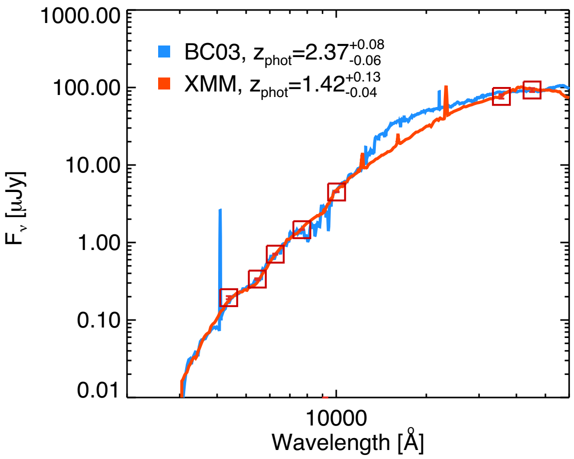

Figure 4. An example of an SED generated by EAZY using star-forming (blue) and AGN (orange) template sets illustrating a degeneracy in $z_{\rm phot}$ solution which occurs for a handful of sources with similar red spectral shapes. The lack of distinctive breaks due to limited photometry make unambiguous identification difficult.

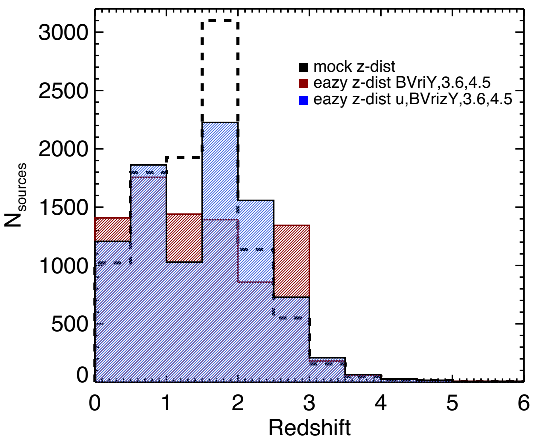

Figure 5. Comparison on the redshift distributions of mock catalogues with and without u- and z'-band data. These two filters are particularly important for picking up the Lyman and Balmer breaks, significant spectral features that inform photometric redshift fitting, at $z < 2$. Exclusion of u- and z'-band data (red distribution) results in a dearth of identifications at $1 < z < 2.5$ and excess at $z < 0.5$ and $z \sim 3$.

not have 3.6 μm detections and as such do not have a prior applied to their photometric redshift solution. The photometric redshifts of the radio sources reported throughout this paper are the median of the distribution produced by the product of the original EAZY PDFs and the prior generated from COSMOS.

4 MOCK CATALOGUE FROM COSMOLOGICAL SIMULATIONS

As a confidence check of our work, we run a mock catalogue of sources, described in Jouvel et al. (2009), through EAZY to understand the validity of EAZY estimated redshifts for given photometric information. The mock catalogue has the same error properties as the OIR data and with it we test the reliability of the photometric redshifts and how improvements can be made, specifically with the introduction of more photometric bands.

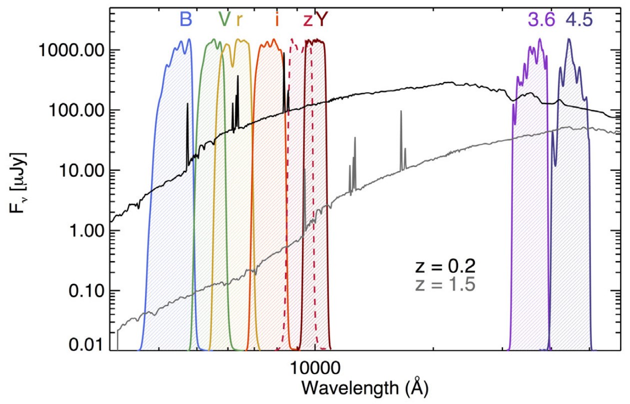

Figure 6. Transmission profiles of Subaru optical (*BVrizY*) and *Spitzer* near-IR (3.6 and 4.5 μm) photometric filters. SEDs of sources with $z = 0.2$ and 1.5 are shown in black and grey respectively. The z'-band profile is dashed to represent the missing z'-band coverage in half of the field. Lack of UV and near-IR coverage makes the accurate identification of $z \sim 1.5$ sources particularly challenging.

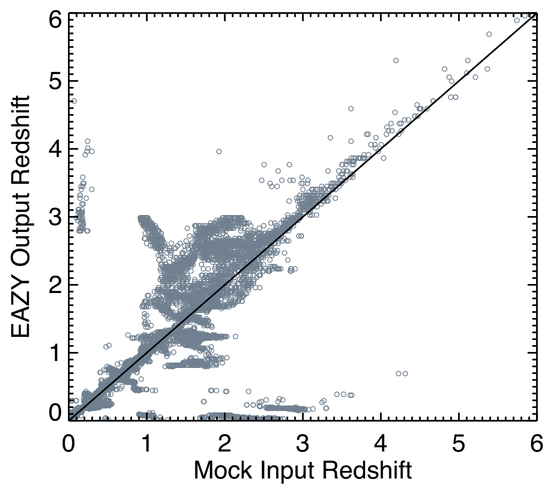

Figure 7. EAZY output photometric redshift versus the input redshift from the mock catalogue using *BVriY*, 3.6 and 4.5 μm photometry. The most common failure modes are $z \sim 1.5$ sources misidentified at $z \sim 1$ and ~ 3.

Fig. 5 illustrates how missing photometric information affects EAZY's ability to generate accurate photometric redshifts. From this, we can see where the estimated photometric redshifts in the SuperCLASS sample might fail. Most noticeably, it struggles to identify $1 < z < 2$ sources. Prominent features in the modelled spectra, e.g. the Lyman and Balmer breaks at 912 and 3646 Å as well as the 4000 Å break, facilitate a more robust identification for EAZY to recover the most accurate redshift estimates. Without observations in the u band, we are missing the Lyman break and Lyman-α emission (1216 Å) at $z < 2$. Similarly, without z' band, we miss the Balmer break from $1.3 < z < 1.5$ and the 4000 Å break from $1 < z < 1.7$. The OIR filter transmission profiles are shown for the bands we have observed in Fig. 6. Two SEDs are shown for a $z = 0.2$ and 1.5 galaxy illustrating where these distinct emission and absorption features lie.

To get a better understanding of how sources might be misidentified by EAZY, we plot the photometric redshift determined by EAZY versus the input redshift from the mock catalogue in Fig. 7 using the star-forming (BC03) templates. This version of the mock

Table 3. Photometric redshifts and radio properties of *e*-MERLIN μJy radio sources.

e-MERLIN name	$z_{\rm phot}$	i' magnitude (AB)	$S_{1.4\,\rm GHz}$ (μJy)	$L_{\rm rad}$ (W Hz^{-1})	Template
SCL-EM-J102355.63+675349.58	$0.63^{+0.03}_{-0.05}$	21.51 ± 0.01	120 ± 12	$(1.10 \pm 0.19) \times 10^{23}$	BC03
SCL-EM-J102155.19+675633.39	$1.88^{+0.43}_{-0.11}$	22.51 ± 0.01	106 ± 14	$(2.03 \pm 0.16) \times 10^{24}$	BC03
SCL-EM-J102609.28+675935.49	$0.33^{+0.04}_{-0.04}$	19.23 ± 0.01	110 ± 13	$(6.75 \pm 0.13) \times 10^{22}$	BC03
SCL-EM-J102608.87+675755.47	$2.34^{+0.23}_{-0.03}$	22.71 ± 0.01	952 ± 27	$(1.98 \pm 0.11) \times 10^{25}$	BC03
SCL-EM-J102545.40+675636.41	$0.45^{+0.04}_{-0.03}$	20.92 ± 0.01	279 ± 8	$(1.34 \pm 0.14) \times 10^{23}$	BC03
SCL-EM-J102651.62+680334.45	$1.53^{+0.08}_{-0.43}$	22.09 ± 0.01	228 ± 12	$(2.76 \pm 0.13) \times 10^{24}$	BC03
SCL-EM-J102609.88+680517.22	$1.78^{+0.16}_{-0.12}$	23.82 ± 0.01	267 ± 12	$(5.91 \pm 0.12) \times 10^{24}$	XMM
SCL-EM-J102520.92+680808.33	$0.87^{+0.02}_{-0.02}$	21.72 ± 0.01	715 ± 33	$(2.73 \pm 0.11) \times 10^{24}$	BC03
SCL-EM-J102150.75+680558.76	$0.23^{+0.01}_{-0.01}$	19.35 ± 0.01	124 ± 12	$(2.14 \pm 0.14) \times 10^{22}$	BC03
SCL-EM-J102714.51+681032.67	$3.03^{+0.15}_{-0.18}$	22.21 ± 0.01	201 ± 10	$(7.19 \pm 0.14) \times 10^{24}$	BC03
...	...	...	...	...	...

Notes: Photometric redshift estimates after applying COSMOS priors, i'-band magnitudes, *e*-MERLIN 1.4 GHz flux densities, and VLA 1.5 GHz radio luminosities of μJy radio sources in the SuperCLASS DR1 field. The template column denotes whether the photometric redshifts were better fit using the star-forming (BC03) or the AGN (*XMM*) templates. The full table consisting of all 149 sources and complete photometric information will be available online.

catalogue incorporates the *BVriY*, 3.6 and 4.5 μm filters, excluding z' band as only half of the DR1 sample has z'-band coverage. This combination of filters matches those used in making the red distribution in Fig. 5. Here, we can see where the biggest disparities occur in our photometric redshift estimates, including many $1 < z < 2$ sources being misidentified at $2 < z < 3$. Furthermore, a non-negligible fraction of $1 < z < 3$ mock galaxies are identified as $z < 0.5$ sources.

We find that close visual inspection of the real data and their galaxy SEDs is the most effective quality check and identify 3 per cent (149/154) of sources with poor photometric redshift fits as stated in Section 3.1.

5 RESULTS

5.1 Redshift distribution

Here, we present the positions of the 149 *e*-MERLIN sources with optical counterparts (matched to OIR counterparts within <1″), their photometric redshifts, i'-band magnitudes and associated errors, *e*-MERLIN flux densities, and VLA radio luminosities (see Table 3). These galaxies span a range of redshifts ($0.2 < z_{\rm phot} < 3.6$) and typically have photometric data from seven of eight OIR filters. Fig. 8 shows the photometric redshift distribution and bootstrap errors of sources with $z_{\rm phot} > 0.5$. We compare this distribution to that of the COSMOS sources which were used as priors in Section 3.3. Finally, we choose to omit the lowest redshift bin as it is known to have an excess of sources due to the presence of the Abell clusters. We see a slight dearth sources between $1 < z < 2$ as well as an excess of sources between $0.5 < z < 1$, $2 < z < 3$, and $z > 3.5$. While our limited photometry may result in some ambiguous redshift identifications (as illustrated in Fig. 4), this was only the case for < 10 per cent of sources.

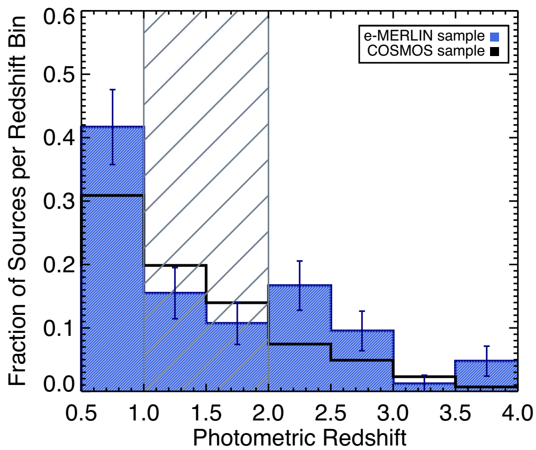

Figure 8. Fraction of sources per redshift bin of *e*-MERLIN sources with OIR counterparts ($i' < 24.5$, blue histogram) compared to the redshift distribution of our comparative sources from COSMOS (black). We have omitted the first redshift bin ($0 < z_{\rm phot} < 0.5$) as it is known to have an excess of sources due to the Abell clusters in the field. The grey hashed region ($1 < z_{\rm phot} < 2$) shows where we find the largest absence of sources due to our current photometric coverage. The excess at $0.5 < z < 1$ is likely boosted by sources sitting at $1 < z < 3$ as suggested by our simulations shown in Fig. 7.

5.2 Radio luminosities

Of the 149 sources, we determine spectral indices (α) for 60 that possess radio detections from both VLA and GMRT (325 MHz). In this paper, we adopt the convention $S \propto \nu^{-\alpha}$ where $\alpha > 0$. Fig. 9 shows the 1.4 GHz VLA flux densities versus α. Errors are propagated given the scatter in flux density. For the remaining galaxies lacking GMRT detections, we determine upper limits on the spectral index based on their VLA detections and the 5 σ detection limit for GMRT (170 μJy beam^{-1}). The spectral index upper limits are denoted as grey arrows. Due to the large number of upper limits, we employ the Kaplan–Meier estimator modified to handle left-censored data (Davidson-Pilon et al. 2019) to produce a cumulative distribution function (CDF) and estimate the median of the combined data and upper limits. Based on this, we can constrain the median of the full sample to be $\langle\alpha\rangle \geq -0.28$ and 80 per cent of the sample has $\alpha < 0.59$. This median value is significantly shallower than spectral indices of star-forming galaxies in the literature. For example, Calistro Rivera et al. (2017) find $\langle\alpha\rangle = 0.74^{+0.27}_{-0.41}$ over the same frequency range. However, our calculated value is driven by

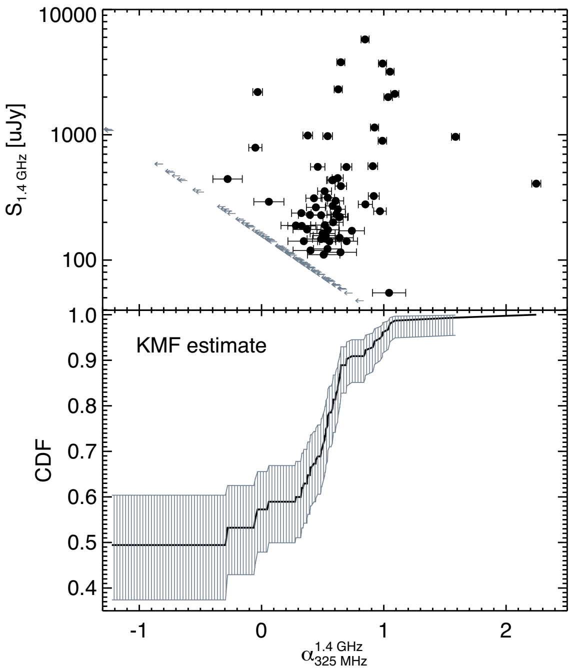

Figure 9. Top*:* 1.4 GHz VLA flux density versus spectral index for galaxies with both VLA and GMRT detections. Grey arrows show spectral index upper limits for sources assuming a 5 σ GMRT detection (170 µJy.) Bottom*:* CDF of calculated spectral indices and upper limits, determined by the Kaplan–Meier estimator.

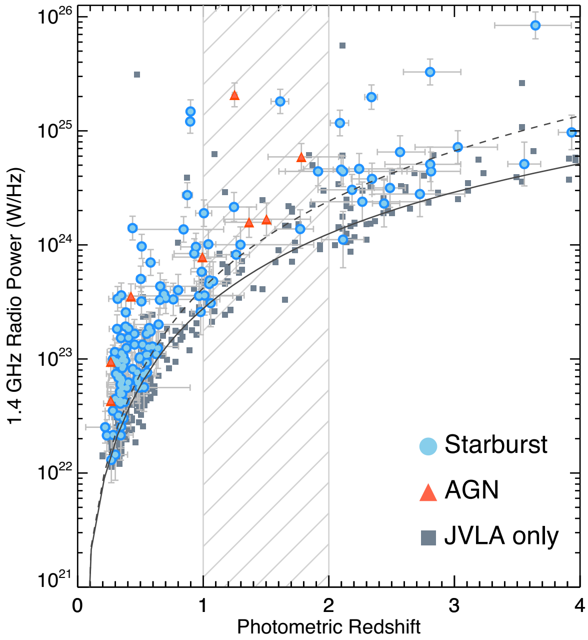

Figure 10. Radio power of the 149 SuperCLASS sources with *e*-MERLIN and OIR detections. The broad range of radio power suggests the presence of both star-forming galaxies and AGN. Blue circles represent sources fit with the BC03 star-forming templates, while orange triangles are sources fit with the *XMM* AGN templates. Grey squares indicate VLA sources with no *e*-MERLIN counterpart. Dark grey lines show selection curves for 5 σ *e*-MERLIN detections assuming a spectral index α of 0.5 (solid line) and 1.1 (dashed line) corresponding to the rough minimum and maximum spectral index of diffuse synchrotron emission from cosmic ray electrons (Lisenfeld & Völk 2000). The grey hatched region replicates the redshift range where we see a modest dearth of objects detected in the full catalogue due to the current photometric band coverage ($1 < z_{\rm phot} < 2$).

the lower limits and we would expect the distribution to shift towards steeper slopes if more GMRT observations became available. The median of the constrained subsample (excluding the upper limits) is $\langle\alpha\rangle = 0.59 \pm 0.04$. This is not representative of the full sample, but it is well within the lower limits of the median value from the literature.

Fig. 10 shows the rest-frame 1.4 GHz radio luminosities of all 149 *e*-MERLIN DR1 radio sources. This sample is detected with both *e*-MERLIN and VLA and we chose to adopt the unresolved VLA flux densities as the total flux given the possibility that *e*-MERLIN may resolve out diffuse emission. VLA sources without *e*-MERLIN counterparts are also shown for comparison.

We convert the VLA flux densities and associated errors to rest-frame radio luminosities and assume a synchrotron spectral index of $\alpha = 0.7$ for sources lacking GMRT detections, as synchrotron radiation is expected to dominate radio emission for most µJy radio sources at frequencies below 30 GHz (Condon 1992). Sources which best fit star-forming templates are shown in blue, while orange denotes sources best fit by AGN templates. The median $z_{\rm phot}$ and $L_{\rm rad}$ of the star-forming versus AGN sources are comparable ($\langle z_{\rm phot}\rangle = 0.53$, $\langle L_{\rm rad}\rangle = 2.43 \times 10^{23}$ W Hz^{-1} for star-forming galaxies and $\langle z_{\rm phot}\rangle = 0.47$, $\langle L_{\rm rad}\rangle = 2.17 \times 10^{23}$ W Hz^{-1} for AGN). Our sample spans a broad range of radio power, covering five orders of magnitude. We plot the 149 sources which have photometric redshift uncertainty $\Delta z/(1+z) < 1$ and find that 8 out of 149 sources ($\sim$5 per cent) are better fit by the AGN templates. This is lower than AGN fractions in the literature (Laird et al. 2010; Georgantopoulos, Rovilos & Comastri 2011; Johnson et al. 2013; Wang et al. 2013), however we have adopted a conservative approach for identifying AGN via photometric redshift fits. We will explore the AGN fraction more fully in a future paper.

If dominated by star formation, we expect these µJy radio sources to correspond to far-IR luminosities of Luminous Infrared Galaxies (LIRGs, 10^{11} L$_\odot$) and Ultraluminous Infrared Galaxies (ULIRGs, 10^{12} L$_\odot$) as we step up in radio power beyond $\sim 6 \times 10^{22}$ W Hz^{-1} at $z \sim 0.25$ (LIRGs) and $\sim 6 \times 10^{23}$ W Hz^{-1} at $z \sim 0.8$ (ULIRGs) respectively. Our sample follows the same progression and extends to higher redshift than previous detailed studies of µJy radio sources (Chapman et al. 2005; Barger et al. 2007).

5.3 $z \sim 0.2$ cluster map

The five Abell clusters in the SuperCLASS field were observed as part of the *ROSAT* All-Sky Survey (Voges et al. 1999). X-ray observations for Abell 968, 981, 998, and 1005 were taken by the Position Sensitive Proportional Counter during the pointed GO phase of the *ROSAT* mission (David, Forman & Jones 1999); the *ROSAT* positions are marked in Figs 1 and 11. An X-ray luminosity measurement for Abell 1006 as well as richness for all five clusters is found in Briel & Henry (1993). Masses can be estimated from the L_X –M_{500} relation as discussed in Peters et al. (2018).

5.3.1 Abell cluster discussion

The Abell catalogue of rich galaxy clusters (Abell 1958; Abell et al. 1989) is an invaluable repository of positions and redshifts of over 4000 galaxy clusters. However, not all of the galaxy clusters listed

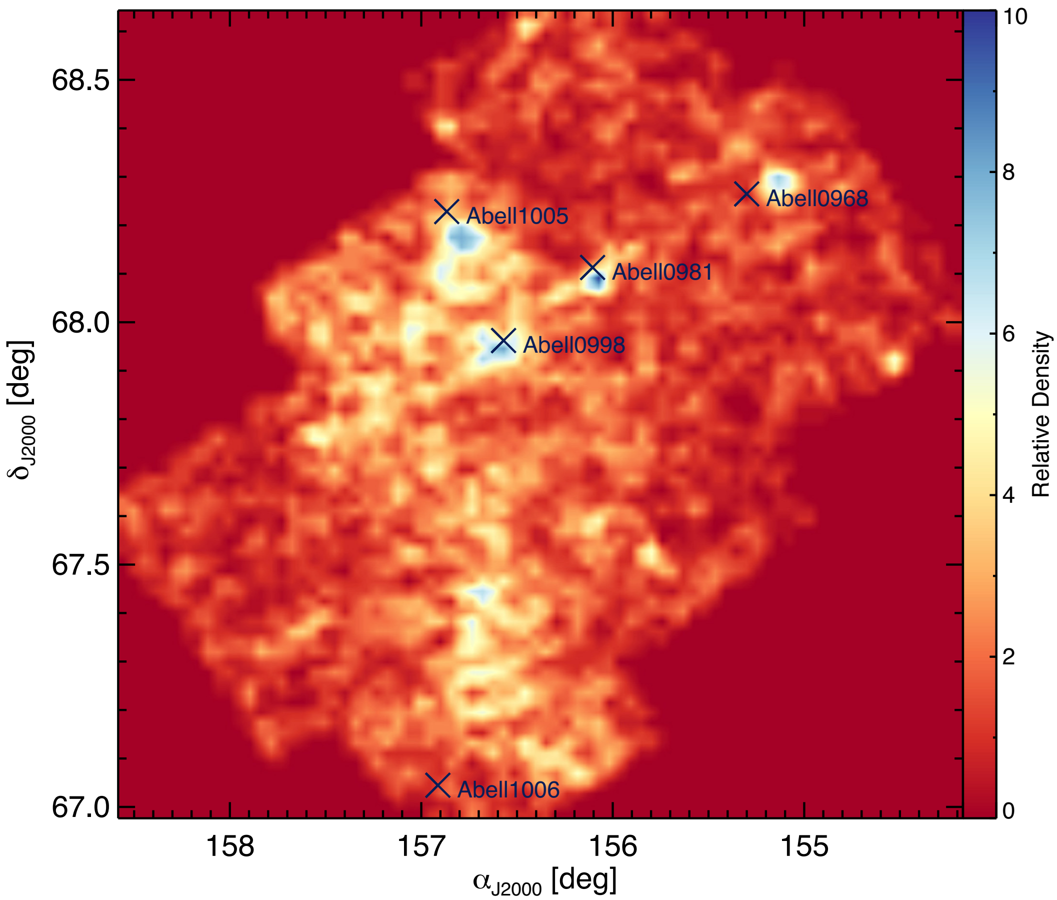

Figure 11. Spatial density of galaxies with $z_{\rm phot} = 0.2 \pm 0.08$ and $i' < 22.5$. Dark blue crosses are centred on the Abell cluster positions from the literature. We count the number of sources within 75 arcsec diameter cells and divide by the mean density across the whole field, resulting in the relative density of sources shown in this figure.

within Abell et al. (1989) are confirmed. The catalogue is based on purely visual surveys of apparent areal densities of galaxies and it is clearly stated the list should not be taken as a definitive list of clusters, but rather a finding list of apparent rich clusters which need further investigation. Furthermore, given the high galactic latitude of the SuperCLASS field, it is unsurprising that information and observations for Abell 968, 981, 998, 1005, and 1006 is lacking.

Redshifts for clusters within the Abell catalogue are an average of all spectroscopic redshifts within the determined counting radius. Struble & Rood (1999) report Abell 968 and 981 have a recorded redshift for only one source, two sources were averaged for Abell 1005, three for Abell 1006, and five sources were averaged for Abell 998. Thus, the cluster redshifts are not well constrained and while the galaxies within them may be spatially concentrated, it is possible that the previously identified spectroscopic sources are not associated with the cluster that could sit at a different redshift. For this reason, we expand our $z_{\rm phot}$ cut to $0.12 < z_{\rm phot} < 0.28$ as stated in Section 5.3.2, otherwise we simply do not recover a significant number of sources to constitute a cluster based on the Abell method (at least 30 sources).

5.3.2 Cluster recovery and analysis

We create a spatial density map of galaxies with photometric redshifts consistent with the reported $z \approx 0.2$ Abell cluster redshifts to investigate whether or not we recover the overdensities spatially using our full photometric redshift catalogue. To allow for even source density across the field which has variable depth, and to ensure robust photometric redshifts, we make a magnitude cut for sources with an i'-band magnitude <22.5 and $z_{\rm phot} = 0.20 \pm 0.08$. The magnitude cut was made to minimize contamination from higher redshift targets with poorly constrained redshifts. We discuss the decision to use this broader range of redshifts even though cluster redshifts are all reported to be within $z = 0.2 \pm 0.005$ in Section 5.3.1. We divide the field into a grid consisting of 75×75 arcsec cells and measure the density of sources within each cell. This is then divided by the mean number of sources per cell across the entire field, resulting in the relative overdensity. We explored several different grid spacings, but settled on 75 arcsec as it provides a smooth distribution of sources across the map and the density of well-constrained sources is high enough to discern overdense environments.

Fig. 11 shows that we successfully recover Abell 968, 981, 998, and 1005 at 7σ, 9σ, 7σ, and $8\,\sigma$ significance respectively, though all are slightly offset from the reported cluster centres based on X-ray emission. We note that there is a spatial offset between *ROSAT* positions and the peak galaxy densities in our density map. While this could possibly be physical – whereby interactions in the supercluster environment lead to shock-heated intracluster medium (ICM) gas offset from the dark matter potentials – a more likely explanation in this context is imprecise astrometric constraints

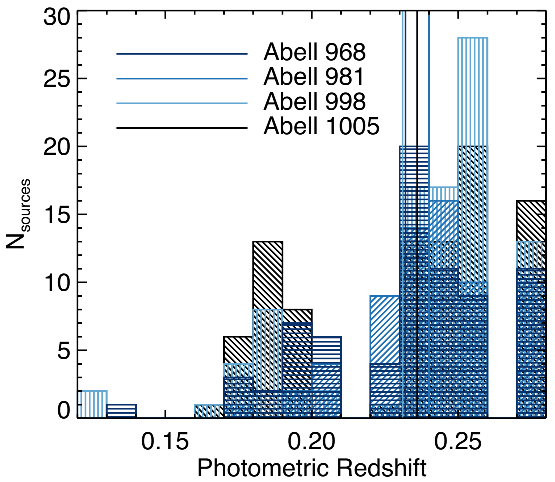

Figure 12. Photometric redshift distribution of sources within 3 arcmin of the cluster centroids determined from Fig. 11. The average $z_{\rm phot}$ of sources around each cluster is listed in Table 4 and shown as vertical lines here.

from *ROSAT* given the 0.5 arcmin beam and few photons used for identification. We also identify one additional high-density region with 6 σ significance at (α, δ)=(156.72,67.45) that is not detected in the existing X-ray data from *ROSAT* (0.1–2.4 keV) or *Suzaku* (0.2–600 keV).

As determined by our mock catalogue analysis (Section 4), there is the potential for an excess of sources to lie at $z_{\rm phot} < 0.5$ due to the current combination of available photometric filters. We create density maps across several redshift slices from $0 < z_{\rm phot} < 0.5$ to determine if the apparent spatial clustering around the cluster positions may be caused by poor photometric redshift fits and projected interlopers rather than the actual presence of a cluster. No redshift slice other than those encompassing our selected range of $0.12 < z_{\rm phot} < 0.28$ produces an overdensity around the distinct cluster positions. The relatively even distribution of sources across the field suggests that even with the inclusion of some poorly fit interlopers, they would not effectively inflate or alter our cluster detections.

We calculate the average cluster photometric redshifts based on sources found within 3 arcmin of the cluster centroids determined from the density map (Fig. 11). The redshift distribution for each cluster is shown in Fig. 12. Errors are quoted as the standard deviation of the peak in the distribution for each cluster. Table 4 summarizes characteristics of the known clusters from the literature and our findings.

A colour–magnitude diagram is shown in Fig. 13. We define cluster member candidates as sources within 3 arcmin of the measured cluster centroids derived from the density map based on the photometric redshifts between $z_{\rm phot} = 0.2 \pm 0.08$. We centre the 3 arcmin apertures on the cluster positions of Abell 968, 9181, 998, and 1005 as they are the largest apparent structures. It is still highly likely that we are including non-cluster members along the line of sight using this method. Sources with $z_{\rm phot}$ within the stated range are shown as black filled circles and referred to as cluster member candidates. Open circles show remaining sources found within the 3 arcmin aperture, but with photometric redshifts inconsistent with the cluster redshifts. We also compare the $B - i'$ versus i' colours of the cluster candidates to all the remaining sources in the SuperCLASS field (grey contours). As expected, galaxies thought to be cluster members lie within a narrower range of colours, along a red sequence of passive galaxies, compared to the broad range of the full sample. We fit a line to sources that appear to fall along this red sequence ($18 < i'$-band<22.5 and $B - i' > 2$) and compare it to the slope determined in Smail et al. (1998) for a $z = 0.24$ galaxy cluster (converted from Vega to AB for a direct comparison). Determining the existence of these five clusters still requires follow-up spectroscopic observations to determine accurate redshifts.

6 SUMMARY

We present photometric redshifts determined from Subaru (*BVrizY*) and *Spitzer* (3.6 and 4.5 μm) photometry of 370 000+ sources (176 000+ with $i' < 24.5$) across the SuperCLASS ∼2 deg^2 field. The SuperCLASS survey will act as a testbed for weak lensing studies as well as a blind search for DSFGs to study their morphological properties from optical through radio wavelengths. We use the 1.4 GHz radio sources in the COSMOS catalogue with similar VLA flux densities and 3.6 μm magnitudes, and well-constrained photometric redshifts as priors to weight the PDFs generated by eazy and further constrain our redshift estimates. Having photometric redshifts is crucial for this survey analysis. Beyond the radio weak lensing goals, we can now more clearly characterize the μJy radio source sample, examine how they may form and evolve across cosmic time, in addition to constraining the source density of these systems.

We also present *e*-MERLIN 1.4 GHz radio luminosities for the first 149 *e*-MERLIN radio sources with optical and near-IR counterparts and robust photometric redshifts in the SuperCLASS DR1 (0.26 deg^2) field. We examine the μJy radio source population in the DR1 survey area, their radio luminosities, and have determined whether the sources are better fit by star-forming or AGN SED templates to account for the expected variation in the types of radio sources in the field. Of the 149 sources, we find 141 starburst galaxies and 8 AGNs, all falling within a redshift range of $0 < z < 4$ and radio luminosities of 10^{21}–10^{25} W Hz^{-1}. We caution that there are likely more AGN in the sample based on literature analysis of the μJy radio galaxy population, but leave further analysis of the AGN content – based on photometry and a morphological analysis – to a future work.

Based on the mock observations we expect some uncertainty in our photometric redshifts and see a slight dearth of sources at $1 < z < 2$ in the full catalogue due to our current wavelength coverage, but plan to rectify this with future observations. Increasing the photometric coverage of the field will reduce the potential to miss easily identifiable spectral features. Obtaining observations in *u* band (∼3000–4000 Å) would allow us to observe the Lyman break from $2.2 < z < 3.2$, providing better identification of higher-z objects as well as Lyman-α emission at $z < 2$. We also believe z' band would be helpful in identifying the Balmer break from $1.1 < z < 1.5$. Future improvements to the SuperCLASS catalogue may come with the addition of observations in these photometric bands as well as spectroscopic follow-up of individual sources which can be used as calibrators for the photometric redshifts.

Creating a spatial density map based on photometric redshifts of $0.12 < z_{\rm phot} < 0.28$ results in the recovery of four (Abell 968, 981, 998, and 1005) out of five suggested Abell clusters in the SuperCLASS field at $> 7\,\sigma$. The cluster candidate galaxies occupy a fairly tight and red region of colour space, indicating their potential cluster membership and evolution to passive galaxies. However, spectroscopic follow-up is required to confirm the presence of these clusters.

Table 4. Observational properties of Abell clusters in SuperCLASS.

Cluster Name	RA_{J2000} (literature)	$Dec._{J2000}$ (literature)	RA (this work)	Dec. (this work)	z_{spec}	z_{phot} (this work)	M_{500} ($M_{\odot}$)	$L_{0.1-2.4keV}$ (erg s^{-1})	Rel. density $N_{cell}/\langle N_{cells}\rangle$
Abell 968*	10:21:09.5	+68:15:53	10:20:31.20	+68:17:24.00	0.195	0.232 ± 0.029	$(1.2 \pm 0.3)\times 10^{14}$	0.401×10^{44}	7
Abell 981*	10:24:24.8	+68:06:47	10:24:19.20	+68:05:23.98	0.201	0.240 ± 0.021	$(2.7 \pm 0.7)\times 10^{14}$	1.670×10^{44}	9
Abell 998*	10:26:17.0	+67:57:44	10:26:19.20	+67:56:59.99	0.203	0.231 ± 0.034	$(1.2 \pm 0.3)\times 10^{14}$	0.411×10^{44}	7
Abell 1005*	10:27:29.1	+68:13:42	10:27:07.19	+68:10:48.00	0.200	0.236 ± 0.033	$(1.0 \pm 0.2)\times 10^{14}$	0.268×10^{44}	8
Abell 1006	10:27:37.2	+67:02:41	–	–	0.204	–	$(2.4 \pm 0.6)\times 10^{14}$	1.320×10^{44}	0

Notes: Cluster information for the five Abell clusters located within the SuperCLASS field. Positions and X-ray luminosities are taken from the BAX data base (Sadat et al. 2004). Redshifts and mass estimates have been collected from Peters et al. (2018). We include the measured centroids from the photometric redshifts as well as the average photometric redshift for each cluster. Errors are quoted as the standard deviation of the N(z) distribution for each cluster. The relative density is the number of sources within a 75 × 75 arcsec cell divided by the mean number of sources per cell obeying the following constraints, i'-band magnitude <22.5 and $z_{phot} = 0.20 \pm 0.08$, across the entire field. *Abell 968, 981, 998, and 1005 are recovered in our spatial density map (Fig. 11).

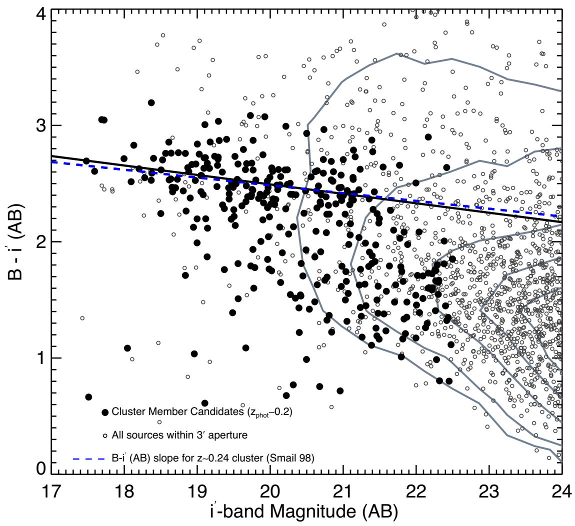

Figure 13. $B - i'$ versus i' colour–magnitude plot of cluster member candidates and SuperCLASS field sources. Cluster member candidates consist of sources found within 3 arcmin of the new measured cluster positions based on the density map with $0.12 < z_{phot} < 0.28$ (filled circles) and open circles are the remaining sources withing the aperture. Grey contours show the colour–magnitude distribution for the entire field. For comparison, we plot the red sequence slope of a $z = 0.24$ galaxy cluster (blue dashed line) determined in Smail et al. (1998) which has been converted from Vega to AB magnitudes.

ACKNOWLEDGEMENTS

The authors thank the reviewer, Kenneth Duncan, for his helpful comments and suggestions. SMM thanks the National Science Foundation for support through the Graduate Research Fellowship under grant Nn. DGE-1610403. PIs of observations: Casey, Battye, Chapman, Sanders, and Scaife. CMC thanks the National Science Foundation for support through grants AST-1714528 and AST-1814034. SMM and CMC thank the University of Texas at Austin College of Natural Sciences for support. In addition, CMC acknowledges support from the Research Corporation for Science Advancement from a 2019 Cottrell Scholar Award sponsored by IF/THEN, an initiative of Lydia Hill Philanthropies. IH and MLB acknowledge the support of a (European Research Council (ERC) Starting Grant (grant no. 280127). IH acknowledges support from the ERC in the form of a Consolidator Grant with number 681431, and from the Beecroft Trust. CAH acknowledges financial support from the European Union's Horizon 2020 research and innovation programme under the Marie Skłodowska-Curie grant agreement no. 705332. Based [in part] on data collected at Subaru Telescope, which is operated by the National Astronomical Observatory of Japan. The authors wish to recognize and acknowledge the very significant cultural role and reverence that the summit of Maunakea has always had within the indigenous Hawaiian community. We are most fortunate to have the opportunity to conduct observations from this mountain. This work is based [in part] on observations made with the *Spitzer Space Telescope*, which is operated by the Jet Propulsion Laboratory, California Institute of Technology under a contract with the National Aeronautics and Space Administration (NASA). The National Radio Astronomy Observatory is a facility of the National Science Foundation operated under cooperative agreement by Associated Universities, Inc. GMRT is run by the National Centre for Radio Astrophysics of the Tata Institute of Fundamental Research. *e*-MERLIN is a National Facility operated by the University of Manchester at Jodrell Bank Observatory on behalf of the Science and Technology Facilities Council (STFC). This research made use of data provided by Astrometry.net.

REFERENCES

Abell G. O., 1958, ApJS, 3, 211
Abell G. O., Corwin H. G., Jr, Olowin R. P., 1989, ApJS, 70, 1
Barger A. J., Cowie L. L., Wang W.-H., 2007, ApJ, 654, 764
Bertin E., Arnouts S., 1996, A&AS, 117, 393
Bezanson R. et al., 2016, ApJ, 822, 30
Bonaldi A., Harrison I., Camera S., Brown M. L., 2016, MNRAS, 463, 3686
Brammer G. B., van Dokkum P. G., Coppi P., 2008, ApJ, 686, 1503
Briel U. G., Henry J. P., 1993, A&A, 278, 379
Brown M. L., Battye R. A., 2011, MNRAS, 410, 2057
Brown M. J. I. et al., 2014, ApJS, 212, 18
Bruzual G., Charlot S., 2003, MNRAS, 344, 1000
Calistro Rivera G. et al., 2017, MNRAS, 469, 3468
Camera S., Harrison I., Bonaldi A., Brown M. L., 2017, MNRAS, 464, 4747
Capak P. et al., 2007, ApJS, 172, 99
Casey C. M. et al., 2012, ApJ, 761, 140
Casey C. M., Narayanan D., Cooray A., 2014, Phys. Rep., 541, 45
Chambers K. C. et al., 2016, preprint (arXiv:1612.05560)
Chapman S. C. et al., 2003, ApJ, 585, 57
Chapman S. C., Blain A. W., Smail I., Ivison R. J., 2005, ApJ, 622, 772
Collaboration P. et al., 2016, A&A, 594, A13
Condon J. J., 1992, ARA&A, 30, 575
Davé R., Finlator K., Oppenheimer B. D., Fardal M., Katz N., Kereš D., Weinberg D. H., 2010, MNRAS, 404, 1355
David L. P., Forman W., Jones C., 1999, ApJ, 519, 533
Davidson-Pilon C. et al., 2019, CamDavidsonPilon/lifelines: v0.22.4
Dekel A., Sari R., Ceverino D., 2009, ApJ, 703, 785
Duncan K. J. et al., 2018, MNRAS, 473, 2655
Engel H. et al., 2010, ApJ, 724, 233

Georgantopoulos I., Rovilos E., Comastri A., 2011, A&A, 526, A46
Gruppioni C. et al., 2013, MNRAS, 432, 23
Harrison I., Camera S., Zuntz J., Brown M. L., 2016, MNRAS, 463, 3674
Helou G., Soifer B. T., Rowan-Robinson M., 1985, ApJ, 298, L7
Hodge J. A., Carilli C. L., Walter F., de Blok W. J. G., Riechers D., Daddi E., Lentati L., 2012, ApJ, 760, 11
Ivison R. J. et al., 2012, MNRAS, 425, 1320
Johnson S. P. et al., 2013, MNRAS, 431, 662
Jouvel S. et al., 2009, A&A, 504, 359
Laigle C. et al., 2016, ApJS, 224, 24
Laird E. S., Nandra K., Pope A., Scott D., 2010, MNRAS, 401, 2763
Lang D., 2009, PhD thesis, University of Toronto, Canada
Lisenfeld U., Völk H. J., 2000, A&A, 354, 423
Madau P., Dickinson M., 2014, ARA&A, 52, 415
Magnelli B., Elbaz D., Chary R. R., Dickinson M., Le Borgne D., Frayer D. T., Willmer C. N. A., 2009, A&A, 496, 57
Nagashima M., Yoshii Y., Totani T., Gouda N., 2002, ApJ, 578, 675
Narayanan D., Hayward C. C., Cox T. J., Hernquist L., Jonsson P., Younger J. D., Groves B., 2010, MNRAS, 401, 1613
Narayanan D. et al., 2015, Nature, 525, 496
Offringa A. R., 2010, Astrophysics Source Code Library, record ascl:1010.017
Offringa A. R., de Bruyn A. G., Biehl M., Zaroubi S., Bernardi G., Pandey V. N., 2010, MNRAS, 405, 155
Peters A., Brown M. L., Kay S. T., Barnes D. J., 2018, MNRAS, 474, 3173
Pickles A. J., 1998, PASP, 110, 863
Quadri R. F., Williams R. J., 2010, ApJ, 725, 794
Riseley C. J. et al., 2016, MNRAS, 462, 917
Sadat R., Blanchard A., Kneib J.-P., Mathez G., Madore B., Mazzarella J. M., 2004, A&A, 424, 1097
Salvato M. et al., 2009, ApJ, 690, 1250
Salvato M. et al., 2011, ApJ, 742, 61
Smail I., Ivison R. J., Blain A. W., 1997, ApJ, 490, L5
Smail I., Edge A. C., Ellis R. S., Blandford R. D., 1998, MNRAS, 293, 124
Struble M. F., Rood H. J., 1999, ApJS, 125, 35
Tacconi L. J. et al., 2008, ApJ, 680, 246
Voges W. et al., 1999, A&A, 349, 389
Wang S. X. et al., 2013, ApJ, 778, 179
Whitaker K. E., Pope A., Cybulski R., Casey C. M., Popping G., Yun M. S., 2017, ApJ, 850, 208

This paper has been typeset from a TEX/LATEX file prepared by the author.